Atmos. Chem. Phys. Discuss., doi:10.5194/acp-2016-691, 2016
Manuscript under review for journal Atmos. Chem. Phys.
Published: 16 August 2016

Atmospheric Chemistry and Physics
Discussions

# Seasonal Prediction of Winter Haze Days in the North-Central North China Plain

Zhicong Yin [1,2], Huijun Wang [1,2,3]

[1]Collaborative Innovation Center on Forecast and Evaluation of Meteorological Disasters/Key Laboratory of Meteorological Disaster, Nanjing University of Information Science & Technology, Nanjing, China
[2]Nansen-Zhu International Research Centre, Institute of Atmospheric Physics, Chinese Academy of Sciences, Beijing, China
[3]Climate Change Research Center, Chinese Academy of Sciences, Beijing, China

*Correspondence to*: Zhicong Yin (yinzhc@163.com)

**Abstract.** Recently, the winter (December–February) haze pollution over the North-Central North China Plain (NCP) has become severe. By treating the year-to-year increment as the predictand, two new statistical schemes were established using the multiple linear regression (MLR) and the generalized additive model (GAM) approaches. By analyzing the associated increment of atmospheric circulation, seven leading predictors were selected to predict the upcoming winter haze days over the NCP ($WHD_{NCP}$). After cross validation, the root mean square error and explained variance of the MLR (GAM) prediction model was 3.39 (3.38) and 53% (54%), respectively. For the final predicted $WHD_{NCP}$, both of these models could capture the interannual and interdecadal trends and the extremums successfully. Independent prediction tests for 2014 and 2015 also confirmed the good predictive skill of the new schemes. The predicted bias of the MLR (GAM) prediction model in 2014 and 2015 was 0.09 (−0.07) and −3.33 (−1.01), respectively. Compared to the MLR model, the GAM model had a higher predictive skill in reproducing the rapid and continuous increase of $WHD_{NCP}$ after 2010.

## 1. Introduction

In recent years, the North-Central North China Plain (NCP; 34–43°N, 114–120°E) has suffered from increasingly severe winter (December–February) haze pollution (Ding et al. 2014), particularly after persistent heavy fog and haze in January 2013 (Zhang et al. 2014; Zhao et al. 2014). After 2000, the combined effects of a rapid increase in total energy consumption and the influence of climate change intensified the haze pollution in central North China (Wang et al. 2016). In conditions of heavy and slowly varying pollutant emissions, the fine particles in the atmosphere reach their saturation levels easily, and the climate conditions become critical contributors of haze. Some new climatic findings have been helpful seasonal predictors of winter haze days over the NCP ($WHD_{NCP}$). The East Asian winter monsoon (EAWM) has a significantly negative relationship with $WHD_{NCP}$ (Yin et al. 2015a; Yin et al. 2015b; Li et al. 2015). By weakening EAWM circulations, negative Sea Surface Temperature (SST) anomalies over the subtropical western Pacific (SWP) could significantly intensify $WHD_{NCP}$ (Yin et al. 2015c). Furthermore, the decline of preceding autumn (Sep–Nov) Arctic Sea Ice (ASI) has led to favorable environments for haze, with high static stability and greatly intensified haze pollution in eastern China (Wang et al. 2015). Although recent studies on the changes in $WHD_{NCP}$ and their associated mechanisms are new and still insufficient, they support the possibility of seasonal prediction.

The climate variables in East Asia showed obvious characteristics of tropospheric biennial oscillation (TBO), based on which, a new interannual increment approach was applied for short-term climate prediction (Wang et al. 2000; Wang et al. 2012). This new approach treated the year-to-year increment of a variable, i.e., the difference between the current and previous year (DY), as the predictand. Because the DY approach utilized the observed information from the previous year and the features of TBO, the interannual variation and interdecadal trend could be captured well. In addition, the signals (i.e., variance) of the predictors and predictand were both amplified (Huang et al. 2015) and, thus, of benefit to improve the prediction skill. If the predictive objects (Y), e.g., haze days, were cross-influenced by socio-economic factors and climatic conditions, the predictand could be represented by $\mathrm{Y} = \mathrm{YS} + \mathrm{YC}$, where YS and YC are the slowly varying socio-economic and climatic components, respectively.

$$\mathrm{DY} = Y_t - Y_{t-1} = (YS_t + YC_t) - (YS_{t-1} + YC_{t-1}) = (YS_t - YS_{t-1}) + (YC_t - YC_{t-1})$$

where the subscripts *t* and *t-1* indicate the current and previous years, respectively.

Commonly, the difference in pollutant emissions between current and previous year was very small, resulting in $(YS_t - YS_{t-1}) \approx 0$, so $\mathrm{DY} \approx (YC_t - YC_{t-1})$. To some extent, the $WHD_{NCP}$ DY reflected the fluctuations caused by climate change. After adding the predicted $WHD_{NCP}$ DY to the observed $WHD_{NCP}$ last year, the interdecadal and socio-economic components were contained in the final prediction. In prior studies, the DY approach has been used to explore the prediction of summer rainfall in China (Fan et al. 2008), heavy winter snow activity in Northeast China (Fan et al.

2013), summer Asian-Pacific Oscillation (Huang et al. 2014) and winter North Atlantic Oscillation (Tian et al. 2015). Furthermore, some variables cross-influenced by socio-economic and climatic factors were predicted successfully using the DY approach, e.g., rice production in Northeast China (Zhou et al. 2014) and the discoloration day for *Cotinus coggygria* leaves in Beijing (Yin et al. 2014). Considering the seriously negative impact of winter haze and the substantial need to predict $WHD_{NCP}$, we made it the goal of this study to apply the DY approach to the seasonal prediction of $WHD_{NCP}$.

The data and methods employed are introduced in section 2. Section 3 describes the predictors and associated circulations. We apply the DY approach to build the prediction models for $WHD_{NCP}$ in section 4. In this section, the statistical models are built based on multiple linear regression (MLR) and generalized additive model (GAM). Then, cross-validation and independent tests are performed to assess the statistical schemes of $WHD_{NCP}$ prediction.

## 2. Datasets and methods

Monthly atmospheric data, such as geopotential height (Z) and surface temperature (TS), are derived from the National Centers for Environmental Prediction/National Center for Atmospheric Research (NCEP/NCAR) global reanalysis dataset with a horizontal resolution of $2.5°\times2.5°$ from 1979 to 2016 (Kalnay et al. 1996). The monthly mean Extended Reconstructed SST datasets with a horizontal resolution of $2^{o}\times2^{o}$ from 1979 to 2016 were obtained from the National Oceanic and Atmospheric Administration (NOAA) (Smith et al. 2008). ASI extent was calculated from the ASI concentration data, downloaded from the Hadley Center with a horizontal resolution of $1^{o}\times1^{o}$ from 1979 to 2016 (Rayner et al. 2003). The monthly gridded soil moisture data from 1979 to 2016 were downloaded from NOAA's Climate Prediction Center (CPC), with a horizontal resolution of $0.5^{o}\times0.5^{o}$ (Huug et al. 2003). The monthly Antarctic Oscillation (AAO) indices from 1979 to 2016 were also obtained from the CPC (Mo et al. 2000).

China ground observations from 39 NCP stations, collected by the National Meteorological Information Center of China 4 times per day from 1979 to 2016, were used to reconstruct the climatic WHD data (Yin et al. 2015c). Here, haze is defined as visibility less than a certain threshold and relative humidity less than 90%. After excluding other weather phenomena affecting visibility, a day with haze at any time is defined as a haze day. Site WHD data were converted into grids after Cressman interpolation (Cressman, 1959), and then the $\mathrm{WHD}_{\mathrm{NCP}}$ was computed as the mean value of the gridded data.

In this study, the statistical models were built based on MLR and GAM methods. The MLR approach, a model-driven method, is ultimately expressed as a linear combination of $K$ predictors ($x_i$) that can generate the least error for prediction of $\hat{y}$ (Wilks 2011). With coefficients $\beta_i$, intercept $\beta_0$ and residual ε, the MLR formula can be described as follows:

$$\hat{y} = \beta_0 + \sum_{i=1}^{K} \beta_i x_i + \varepsilon \qquad (1)$$

The GAM approach is more advanced and was developed from MLR and the generalized linear model (GLM) (Hastie et al. 1990). This data-driven method is particularly effective at handling the complex non-linear and non-monotonous relationships between the predictand and the predictors, whose expressions are replaced by smooth functions (s). Similar to GLM, the dependent variable in GAM can have different probability distributions, such as Gaussian, Poisson, and Binomial, any of which can be transferred by the link function (g). The GAM can be written in the form:

$$g(\hat{y}) = \beta_0 + \sum_{i=1}^{K} \beta_i s(x_i) + \varepsilon \qquad (2)$$

The normalized datasets from 1979 to 2013 were trained as the basic samples to fit the models, and those from 2014 to 2015 were treated as test data for independent prediction. Thereafter, the root mean standard error (RMSE), mean absolute error (MAE) and explained variance (EV) were calculated for evaluation by simple fitting and leave-one-out cross validation.

## 3. The predictors and associated circulations

To choose the DY predictors, the correlated DY atmospheric circulations were identified, as shown in Figure 1. The positive phase of the East Atlantic/West Russia (EA/WR; Barnston et al. 1987) and Pacific Japan (PJ; Nitta 1987) patterns and the negative phase of the Eurasia (EU; Wallace et al. 1981) pattern were obvious, and we took the anti-cyclone circulation over North China as an intermediary leading to a more stable atmosphere. The positive anomaly over the NCP could confine the particles within a thinner boundary layer by suppressing vertical movement and induce an easterly to weaken the East Asia Jet Stream (EASJ), producing weaker cold air. Meanwhile, the water vapor transportation was also enhanced, creating favorable conditions for more $WHD_{NCP}$ than in the previous year.

The pivotal local anti-cyclone over the NCP was the most important contributor; we therefore speculated that pre-autumn TS DY around the NCP should be effective to impact $WHD_{NCP}$ DY. There were significantly negative correlations between $WHD_{NCP}$ DY and pre-autumn TS DY from the Japan Sea to the Stanovoy Range (35–65°N, 130–140°E), the area mean of which was selected as predictor $x_1$ (Figure 2). The correlation coefficient (CC) between $WHD_{NCP}$ DY and predictor $x_1$ was −0.47, exceeding a 99% confidence level. The circulations associated with predictor $x_1$ (×−1) presented obvious features of the negative EU and positive PJ patterns (Figure 3), similar to those shown in Figure 1.

The pre-autumn SST anomalies of the Pacific could influence $WHD_{NCP}$ significantly via the air-sea interaction (Yin et al. 2015c). Figure 4 shows the CC between $WHD_{NCP}$ DY and pre-autumn SST DY. The most significant CC was distributed around the Alaska Gulf (36–56°N, 130–170°W), and the area-averaged SST DY here was defined as predictor $x_2$, whose CC with $WHD_{NCP}$ DY was 0.47, above the 99% confidence level. The positive SST DY around the Alaska Gulf closely correlated with the atmospheric teleconnection patterns, i.e., the positive phases of the EA/WR and PJ and the negative EU patterns intensified haze pollution over the NCP (Figure 5).

Prior studies have documented that the triple SST pattern was a dominant mode of the northern Atlantic in autumn. When the pre-autumn SST anomalies were distributed in a "+−+" pattern from south to north, the subsequent EAWM was stronger, and the surface temperature of North China was lower (Shi 2009). Similarly, the CC between $WHD_{NCP}$ DY and pre-autumn SST DY of the Atlantic was distributed in a "−+−" pattern (Figure 6). The area-averaged SST DY of the northern center was defined as predictor $x_3$, whose CC with $WHD_{NCP}$ DY was −0.50, passing the 99% confidence test. The most obvious DY atmospheric circulations related with predictor $x_3$ (×−1) were the negative EU pattern, whose south center linked with a subtropical high (Figure 7). The continental high and marine low were both weaker, leading to weaker EAWM and weaker cold air. The pressure gradient over the east coast of China also resulted in a southerly anomaly, indicating smaller surface wind and more moisture and resulting in more $WHD_{NCP}$.

ASI decreased dramatically with significant variance and was a significant contributor influencing $WHD_{NCP}$ in eastern

China (Wang et al. 2015; Wang et al. 2016). The CC between pre-autumn ASI DY and WHD$_{NCP}$ DY was calculated (Figure 8) and was significantly positive around Beaufort Sea (73–78°N, 130–165°W). The area-averaged ASI extent DY of Beaufort Sea was selected as the fourth predictor ($x_4$), and its CC with WHD$_{NCP}$ DY was 0.37, above a 95% confidence level. A positive center was located over the Central Siberian and Mongolia Plateau, and negative centers were distributed zonally from southern China to the subtropical Pacific (Figure 9). Thus, the EAJS was weakened by the induced easterly.

Soil moisture is an important factor for seasonal prediction, but only after SST (Guo et al. 2007). The questions with respect to soil moisture were whether pre-summer or autumn soil moisture would be effective for seasonal prediction of WHD$_{NCP}$ DY. The area-averaged pre-autumn soil moisture DY of the Bohai rim (35–42°N, 117–127°E), defined as predictor $x_5$, showed a significantly negative correlation with WHD$_{NCP}$ DY, i.e., the CC was −0.59, exceeding a 99% confidence test (Figure 10). The CC between predictor $x_5$ and Z500 (Z at 500 hPa) was distributed in a similar way as in Figure 1. The positive EA/WR and PJ phases and the negative EU phase was obvious and led to more WHD$_{NCP}$ than in the previous year (Figure 11). As shown in Figure 12, the pre-summer soil moisture DY in the east of Mongolia (48–52°N, 115–125°E) also had a close relationship with WHD$_{NCP}$ and with WHD$_{NCP}$ DY. The area-averaged soil moisture DY in the east of Mongolia was defined as predictor $x_6$, whose CC with WHD$_{NCP}$ DY was 0.41, above a 95% confidence level. The negative EU pattern could be recognized from the associated atmospheric circulation with predictor $x_6$ (Figure 13), which intensified the haze pollution over the NCP.

Recently, some studies documented that Antarctic Oscillation (AAO) could affect the East Asian climate through cross-equatorial flow, e.g., the Somali jet (Fan et al. 2004; Fan et al. 2006; Fan et al. 2007a; Fan et al. 2007b). After the late-1990s, global sea level pressure and Z300 in boreal January were characterized by the concurrence of the Aleutian low and the negative phase of the AAO (Li et al. 2014). We investigated the relationship between WHD$_{NCP}$ DY and Z850 in the Southern Hemisphere and found that the distribution was remarkably similar to that of the negative phase of AAO (Figure 14). Furthermore, the CC between the Sep–Oct AAO DY and WHD$_{NCP}$ DY was −0.54, exceeding a 99% confidence test. As shown in Figure 15, the positive phases of the EA/WR and PJ patterns were closely correlated with the negative phase of Sep–Oct AAO and were responsible for more WHD$_{NCP}$ than in the previous year. Hence, the Sep–Oct mean AAO index was selected as the last predictor ($x_7$) to forecast the interannual increment of WHD$_{NCP}$.

## 4. The prediction models and validations

In total, seven DY predictors ($x_1, x_2 \ldots, and\ x_7$) were chosen to build the seasonal prediction model (SPM) for $\mathrm{WHD_{NCP}}$ DY (Table 2). Among the predictors were 21 types of pair combinations, of which only 5 presented significant linear correlation (Figure 16). The multicollinearity would not be a problem when modeling with the MLR approach. Although the linear correlation between the predictand and each predictor was significant, the non-linear interaction would also affect the $\mathrm{WHD_{NCP}}$ and should be taken into account. In this section, seasonal prediction models were established using MLR ($\mathrm{SPM_{MLR}}$) and GAM ($\mathrm{SPM_{GAM}}$) and validated in detail.

The $\mathrm{WHD_{NCP}}$ DY showed obvious features of biennial oscillation (Figure 17), illustrating the DY approach was suitable for its prediction. The $\mathrm{SPM_{MLR}}$ of $\mathrm{WHD_{NCP}}$ DY was as follows:$\mathrm{DY}/10 = -2.774x_1 + 2.582x_2 - 1.631x_3 + 2.528x_4 - 2.229x_5 + 2.555x_6 - 1.812x_7$. After cross validation, the $\mathrm{RMSE_{CV}}$ of $\mathrm{SPM_{MLR}}$ was 3.39 days, and the CC between fitted and observed $\mathrm{WHD_{NCP}}$ DY was 0.73, accounting for 53% of the total variance (Table 2). The percentage of same sign (PSS; same sign means the mathematical sign of the fitted and observed $\mathrm{WHD_{NCP}}$ DY was the same) was 79.4%. The $\mathrm{SPM_{MLR}}$ showed good ability to predict the negative and least $\mathrm{WHD_{NCP}}$ DY but did not adequately capture the continuous positive value after 2011 (Figure 17a). The fitted $\mathrm{WHD_{NCP}}$ DY from 2011 to 2013 varied similarly to that before 2010 and did not reflect the rising trend after 2010. As an independent prediction test, the predicted bias in 2014 was 0.09, illustrating good performance, but the bias in 2015 was larger, i.e., −3.33.

We also applied the GAM approach to build a prediction model that would contain the non-linear relationship with smooth functions. The $\mathrm{SPM_{GAM}}$ of $\mathrm{WHD_{NCP}}$ DY was as follows: $\mathrm{DY}/10 = -2.164\mathrm{s}(x_1) + 2.036\mathrm{s}(x_2) - 1.721x_3 + 2.588\mathrm{s}(x_4) - 2.157\mathrm{s}(x_5) + 2.187x_6 - 2.506x_7$. During the simple fitting, the $\mathrm{SPM_{GAM}}$ performed very well. The RMSE was 1.56 days, and the CC between the fitted and observed $\mathrm{WHD_{NCP}}$ DY was 0.95. The $\mathrm{SPM_{GAM}}$ could fit the minimum (in 2003) and maximum (in 2013), and show the trend well, indicating an advantage to processing the non-linear relationship. After cross validation, the performance of $\mathrm{SPM_{GAM}}$ decreased dramatically, meaning that its stability was worse than that of $\mathrm{SPM_{MLR}}$. The $\mathrm{RMSE_{CV}}$ of $\mathrm{SPM_{GAM}}$ was 3.38 days and the CC between fitted and observed $\mathrm{WHD_{NCP}}$ DY was 0.74, accounting for 54% of the total variance (Table 2). The PSS of $\mathrm{SPM_{GAM}}$ results was 73.5%, which is close to the result from

$SPM_{MLR}$. The $SPM_{GAM}$ also showed good ability to predict the negative and minimum $WHD_{NCP}$ DY and better performance to fit the maximum in 2013 (Figure 17b). The predicted bias in 2014 and 2015 was −0.07 and −1.01, results that are better than those from $SPM_{MLR}$. The CC between the bias of $SPM_{MLR}$ and $SPM_{GAM}$ from 1980 to 2013 was 0.83, above a 99.99% confidence level. If the $SPM_{MLR}$ performed well in some years, the $SPM_{GAM}$ also showed good ability in these years, and *vice versa*. We speculated that the reason was that some useful factors were not diagnosed and included here.

After adding the predicted $WHD_{NCP}$ DY to the observed information in the previous year, the predicted $WHD_{NCP}$ in the current year was obtained. For example, the predicted $WHD_{NCP}$ DY in 2012 was added to the measured $WHD_{NCP}$ in 2011, and the result was the final predicted $WHD_{NCP}$ in 2012. In Figure 18, the simulative $WHD_{NCP}$ anomaly was fitted by cross-validation from 1980 to 2013 and predicted in 2014 and 2015. For $SPM_{MLR}$ and $SPM_{GAM}$, the CC between the original (detrended) observed and simulative $WHD_{NCP}$ was 0.89 (0.87) and 0.90 (0.88), respectively. Both of these prediction models could capture the interannual and interdecadal trend and the extremums. The PSS of the anomalies from the two models was 100%, meaning these two models could predict the sign of $WHD_{NCP}$ anomaly successfully. The $SPM_{GAM}$ could simulate the abrupt rising trend in 2010 better than $SPM_{MLR}$, which was important for the prediction of recent years.

## 5. Conclusions and Discussions

In this paper, we treated the $WHD_{NCP}$ DY as the predictand and built two prediction models using the MLR and GAM approach. In the DY atmospheric circulation, the positive phases of the EA/WR and PJ patterns and the negative phase of the EU pattern intensified the haze pollution by inducing positive anomalies over the NCP. Finally, seven leading predictors were selected and are listed in Table 2.

After cross validation, the $RMSE_{CV}$ and explained variance of $SPM_{MLR}$ ($SPM_{GAM}$) was 3.39 (3.38) and 53% (54%). The PSS of these two prediction models was also similar, i.e., more than 73%. The $WHD_{NCP}$ DY increased rapidly and persistently after 2010, and the $SPM_{GAM}$ could capture this trend better. For the final predicted $WHD_{NCP}$, both of these prediction models could capture the interannual and interdecadal trends and the extremums. The PSS of the anomalies from two models was 100%, and the $SPM_{GAM}$ simulated the abrupt increase in 2010 better than $SPM_{MLR}$. The predicted bias of

$SPM_{MLR}$ ($SPM_{GAM}$) in 2014 and 2015 was 0.09 (−0.07) and −3.33 (−1.01), respectively. Both of these models performed well in independent tests, but the biases of $SPM_{GAM}$ were smaller.

Although these two statistical models performed well during most of the past 3 decades and could predict the $WHD_{NCP}$ in 2014 and 2015 with small biases, they showed disadvantages when simulating the rapid rising trend after 2010. If the $SPM_{MLR}$ performed well in some years, the $SPM_{GAM}$ also showed good ability in these years, and *vice versa*. One possible reason could be that some useful factors were not diagnosed and included here. In this paper, we assumed that the difference in pollutant emissions between current and previous years was very small and that the socio-economic component of $WHD_{NCP}$ varied slowly. Another possible reason might be that in certain years, this pollutant emission proportion varied rapidly.

## Acknowledgement

This research was supported by the National Natural Science Foundation of China (Grants: 41421004 and 41210007) and CAS-PKU Partnership Program.

## References

Barnston A G, Livezey R E. 1987. Classification, seasonality and persistence of low frequency atmospheric circulation patterns. Mon. Wea. Rev., 115: 1083–1126.

Cressman G. 1959. An operational objective analysis system. Mon. Wea. Rev. 87(10): 367–374.

Ding Y H, Liu Y J. 2014. Analysis of long-term variations of fog and haze in China in recent 50 years and their relations with atmospheric humidity. Sci. China Ser. D: Earth Sci. 57: 36–46(in Chinese).

Fan K, Tian B Q. 2013. Prediction of wintertime heavy snow activity in Northeast China. Chinese Science Bulletin. 58(12): 1420–1426.

Fan K, Wang H J, Choi Y J. 2008. A physically-based statistical forecast model for the middle-lower reaches of Yangtze River Valley summer rainfall. Chinese Science Bulletin. 54(4)：602–609

Fan K, Wang H J. 2006. Studies of the relationship between Southern Hemispheric atmospheric circulation and climate over East Asia. Chinese journal of Atmosphere Sciences, 20: 402–412

Fan K, Wang H J. 2007a. Simulation on the AAO anomaly and its influence on the Northern Hemispheric circulation in boreal winter and spring. Chinese Journal of Geophysics, 50: 397–403

Fan K, Wang H J. 2007b. Dust storms in North China in 2002: A case study of the low frequency oscillation. Adv. Atmos. Sci., 24: 15–23

Fan K, Wang H J. 2004. Antarctic oscillation and the dust weather frequency in North China. Geophys. Res. Lett., 31, L10201, doi:10.1029/2004GL019465

Guo W D, Ma Z G, Wang H J. 2007. Soil moisture—an important factor of seasonal precipitation prediction and its application. Climatic and Environmental Research, 12 (1): 20–28

Hastie T J, Tibshirani R J. 1990. Generalized Additive Models. Chapman & Hall, London.

Huang R H. 1992. The East Asia/Pacific pattern teleconnection of summer circulation and climate anomaly in East Asia. J. Meter. Res., 6: 25–37

Huug D, Huang J, Fan Y. 2003. Performance and Analysis of the constructed analogue method applied to US soil moisture applied over 1981–2001. J. of Geophysical Research. 108: 1–16.

Kalnay E, Kanamitsu M, Kistler R, Collins W, Deaven D, Gandin L, Iredell M, Saha S, White G, Woollen J, Zhu Y, Leetmaa A,Reynolds R, Chelliah M, Ebisuzaki W, Higgins W, Janowiak J,Mo KC, Ropelewski C, Wang J, Jenne R, Joseph D. 1996. The NCEP/NCAR 40-year reanalysis project. Bull. Am. Meteorol. Soc., 77: 437–471, doi: 10.1175/1520-0477(1996)077<0437: TNYRP>2.0.CO; 2.

Li F, Wang H J, Gao Y Q. 2015. Modulation of Aleutian low and Antarctic oscillation co-variability by ENSO. Climate Dynamics, 44: 1245–1256

Li Q, Zhang R H, Wang Y. 2015. Interannual variation of the winter-time fog–haze days across central and eastern China and its relation with East Asian winter monsoon. Int. J. Climatol. 36 (1): 346–354, doi: 10.1002/joc.4350.

Mo K. C. 2000. Relationships between Low-Frequency Variability in the Southern Hemisphere and Sea Surface Temperature Anomalies. J. Climate, 13, 3599–3610

Nitta T. 1987. Convective activities in the tropical western Pacific and their impact on the Northern Hemisphere summer circulation. J. Meteor. Soc. Japan, 64: 373–390.

Rayner N A, Parker D E, Horton E B, Folland C K, Alexander L V, Rowell D P, Kent E C, Kaplan A. 2003. Global analyses of sea surface temperature, sea ice, and night marine air temperature since the late nineteenth century. J. Geophys. Res. 108 (14): 4407 doi: 10.1029/2002JD002670

Shi X L. 2014. The impact of mid-high latitude oceans on climate change over north and northeast China. Qing Dao: Ocean University of China, 1 pp.

Smith T, Reynolds R, Peterson T, Lawrimore J. 2008. Improvements to NOAA's historical merged land–ocean surface temperature analysis (1880–2006). J. Climat., 21: 2283–2296

Tian B Q, Fan K. 2015. A skillful prediction model for winter NAO based on Atlantic sea surface temperature and Eurasian snow cover, Weather and Forecasting. 30: 197–204

Wallace J M, Gutzler D S. 1981. Teleconnection in the geopotential height field during the Northern Hemisphere winter. Mon. Wea. Rev., 109, 784–812, doi:10.1175/1520-0493(1981)109,0784:TITGHF.2.0.CO;2.

Wang H J, Chen H P, Liu J P. 2015. Arctic sea ice decline intensified haze pollution in eastern China. Atmos. Oceanic Sci. Lett., 8 (1): 1–9

Wang H J, Chen H P. 2016. Understanding the recent trend of haze pollution in eastern China: role of climate change. Atmos. Chem. Phys., 16: 4205–4211

Wang H J, Fan K, Lang X M, Sun J Q, Chen L J. 2012. Advances in climate prediction theory and technique of China, Beijing: China Meteorological Press. 120–140 (in Chinese).

Wang H J, Zhou G Q, Zhao Y. 2000. An effective method for correcting the seasonal-interannual prediction of summer climate anomaly. Adv. Atmos. Sci., 17 (2), 234–240

Wilks D S. 2011. Statistical methods in the atmospheric sciences. Academic press, 1 pp.

Yin Z C, Wang H J, Guo W L. 2015a. Climatic change features of fog and haze in winter over North China and Huang-Huai Area. SCIENCE CHINA Earth Sciences, 58(8): 1370–1376.

Yin Z C, Wang H J. 2015c. The relationship between the subtropical Western Pacific SST and haze over North-Central North

Atmos. Chem. Phys. Discuss., doi:10.5194/acp-2016-691, 2016
Manuscript under review for journal Atmos. Chem. Phys.
Published: 16 August 2016

China Plain. International Journal of Climatology, DOI: 10.1002/joc.4570

Yin Z C, Yuan D M, Ding D P, Xie Z. 2014. Statistical prediction based on meteorology of Cotinus Coggygria leaves discoloration-day in the Fragrant hill, Meteorological Monthly, 40 (2): 229–233 (in Chinese)

Yin Z C, Wang H J, Yuan D M. 2015b. Interdecadal increase of haze in winter over North China and the Huang-huai area and the weakening of the East Asia winter monsoon. Chin. Sci. Bull. 60(15): 1395–1400 (in Chinese).

Zhang R H, Li Q, Zhang R N. 2014. Meteorological conditions for the persistent severe fog and haze event over eastern China in January 2013. Science China: Earth Sciences, 57: 26–35. doi: 10.1360/972013-150

Zhao N, Yin Z C, Wu F. 2014. Characteristics of persistent fog and haze process and its forming reason in Beijing. J. Meteorol. Environ. 30(5): 15–20 (in Chinese).

Zhou M Z, Wang H J. 2014. Late winter sea ice in Bering Sea: predictor for maize and rice production in Northeast China, Journal of applied Meteorology and Climatology, 53: 1183–1192

**Table and Figure Captions:**

**Table 1**. The RMSE, MAE, CC and EV of MLR and GAM models, and predicted bias for 2014 and 2015. The subscripts “S” and “CV” indicated simple and cross-validation fitting.

**Table 2**. The predictors and their meaning. “CC” indicated the correlation coefficient between predictor and $\mathrm{WHD_{NCP}}$ DY from 1980 to 2013.

**Figure 1**. The correlation coefficient (CC) between $\mathrm{WHD_{NCP}}$ DY and Z500 DY in winter from 1980 to 2013. The white curves indicate that the CC exceeded the 95% confidence level. A and C represent anti-cyclone and cyclone, respectively.

**Figure 2**. The CC between $\mathrm{WHD_{NCP}}$ DY and TS DY in autumn from 1980 to 2013. The shades indicate that the CC exceeded the 95% confidence level, and the rectangle represents the selected region (35–65°N，130–140°E) of predictor $x_1$.

**Figure 3**. The CC between predictor $x_1$ (×−1) and Z500 DY in winter from 1980 to 2013. The white curves indicate that the CC exceeded the 95% confidence level. A and C represent anti-cyclone and cyclone, respectively.

**Figure 4**. The CC between $\mathrm{WHD_{NCP}}$ DY and Pacific SST DY in autumn from 1980 to 2013. The shades indicate that the CC exceeded the 95% confidence level, and the rectangle represents the selected region (36–56°N，130–170°W) of predictor $x_2$.

**Figure 5**. The CC between predictor $x_2$ and Z500 DY in winter from 1980 to 2013. The white curves indicate that the CC exceeded the 95% confidence level. A and C represent anti-cyclone and cyclone, respectively.

**Figure 6**. The CC between $\mathrm{WHD}_{\mathrm{NCP}}$ DY and Atlantic SST DY in autumn from 1980 to 2013. The shades indicate that the CC exceeded the 95% confidence level, and the rectangle represents the selected region (50–70°N，30–65°W) of predictor $x_3$.

**Figure 7**. The CC between predictor $x_3$ (×−1) and Z500 DY in winter from 1980 to 2013. The white curves indicate that the CC exceeded the 95% confidence level. A and C represent anti-cyclone and cyclone, respectively.

**Figure 8**. The CC between $\mathrm{WHD}_{\mathrm{NCP}}$ DY and ASI DY in autumn from 1980 to 2013. The shades indicate that the CC exceeded the 95% confidence level, and the rectangle represents the selected region (73–78°N，130–165°W) of predictor $x_4$.

**Figure 9**. The CC between predictor $x_4$ and Z500 DY in winter from 1980 to 2013. The white curves indicate that the CC exceeded the 95% confidence level.

**Figure 10**. The CC between $\mathrm{WHD}_{\mathrm{NCP}}$ DY and SoilM DY in autumn from 1980 to 2013. The shades indicate that the CC exceeded the 95% confidence level, and the rectangle represents the selected region (35–42°N，117–127°E) of predictor $x_5$.

**Figure 11**. The CC between predictor $x_5$ (×−1) and Z500 DY in winter from 1980 to 2013. The white curves indicate that the CC exceeded the 95% confidence level. A and C represent anti-cyclone and cyclone, respectively.

**Figure 12**. The CC between $\mathrm{WHD}_{\mathrm{NCP}}$ DY and SoilM DY in summer from 1980 to 2013. The shades indicate that the CC exceeded the 95% confidence level, and the rectangle represents the selected region (48–52°N，115–125°E) of predictor $x_6$.

**Figure 13.** The CC between predictor $x_6$ and Z500 DY in winter from 1980 to 2013. The white curves indicate that the CC exceeded the 95% confidence level. A and C represent anti-cyclone and cyclone, respectively.

**Figure 14.** The CC between $\mathrm{WHD}_{\mathrm{NCP}}$ DY and Sep–Oct Z850 DY from 1980 to 2013. The white curves indicate that the CC exceeded the 95% confidence level.

**Figure 15.** The CC between predictor $x_7$ (×−1) and Z500 DY in winter from 1980 to 2013. The white curves indicate that the CC exceeded the 95% confidence level.

**Figure 16.** Correlogram of the dependent (Y) and independent ($x_1, x_2 \ldots, \boldsymbol{and}\ x_7$) variables, whose names were written on the diagonal. The lower panel shows the pie charts of correlation coefficients, representing the values by area and saturation, and showing positive/negative sign by blue/red, respectively. The upper panel shows the scatter plots.

**Figure 17.** The temporal variation of measured (black) $WHD_{NCP}$ DY, MLR (red, a) and GAM (red, b) cross-validation fitted $WHD_{NCP}$ DY from 1980 to 2013. The results for 2014 and 2015 represent the measured (black square) and predicted (red hollow circle) $WHD_{NCP}$ DY.

**Figure 18.** The temporal variation of measured (black) $WHD_{NCP}$ anomaly from 1980 to 2015, MLR (blue) and GAM (red) simulative $WHD_{NCP}$ anomaly, which was composed of cross fitted series from 1980 to 2013 and predicted values in 2014 and 2015.

**Table 1: The RMSE, MAE, CC and EV of MLR and GAM models, and predicted bias for 2014 and 2015. The subscripts "S" and "CV" indicated simple and cross-validation fitting.**

| | $MLR_s$ | $MLR_{CV}$ | $GAM_s$ | $GAM_{CV}$ |
|---|---|---|---|---|
| **RMSE** | 2.39 | 3.39 | 1.56 | 3.38 |
| **MAE** | 1.75 | 2.37 | 1.10 | 2.58 |
| **CC** | 0.87 | 0.72 | 0.95 | 0.74 |
| **EV** | 76% | 53% | 90% | 54% |
| **$Bias_{14}$** | 0.09 | | −0.07 | |
| **$Bias_{15}$** | −3.33 | | −1.01 | |

**Table 2. The predictors and their meaning. "CC" indicated the correlation coefficient between predictor and WHD$_{NCP}$ DY from 1980 to 2013.**

| Predictors | Meaning | CC |
|---|---|---|
| $x_1$ | pre-autumn TS DY from Japan Sea to Stanovoy Range | −0.47 |
| $x_2$ | pre-autumn SST DY around Alaska Gulf | 0.47 |
| $x_3$ | pre-autumn SST DY to the south of Greenland | −0.50 |
| $x_4$ | pre-autumn ASI extent DY of Beaufort Sea | 0.37 |
| $x_5$ | pre-autumn soil moisture DY of the Bohai rim | −0.59 |
| $x_6$ | pre-summer soil moisture DY in the east of Mongolia | 0.41 |
| $x_7$ | Sep–Oct AAO index DY | −0.54 |

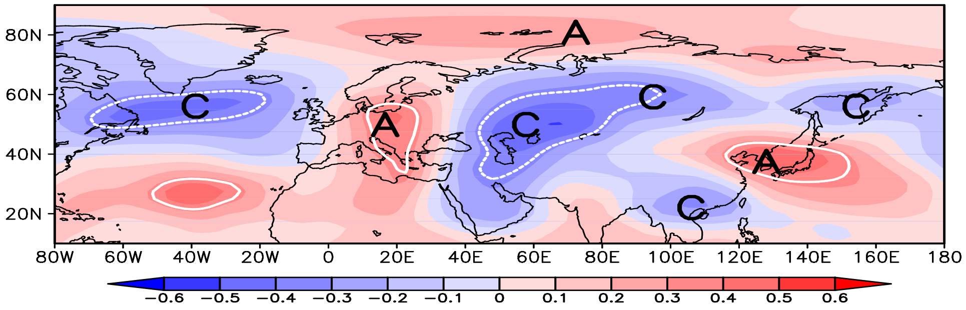

**Figure 1. The correlation coefficient (CC) between WHD$_{NCP}$ DY and Z500 DY in winter from 1980 to 2013. The white curves indicate that the CC exceeded the 95% confidence level. A and C represent anti-cyclone and cyclone, respectively.**

Atmos. Chem. Phys. Discuss., doi:10.5194/acp-2016-691, 2016
Manuscript under review for journal Atmos. Chem. Phys.
Published: 16 August 2016

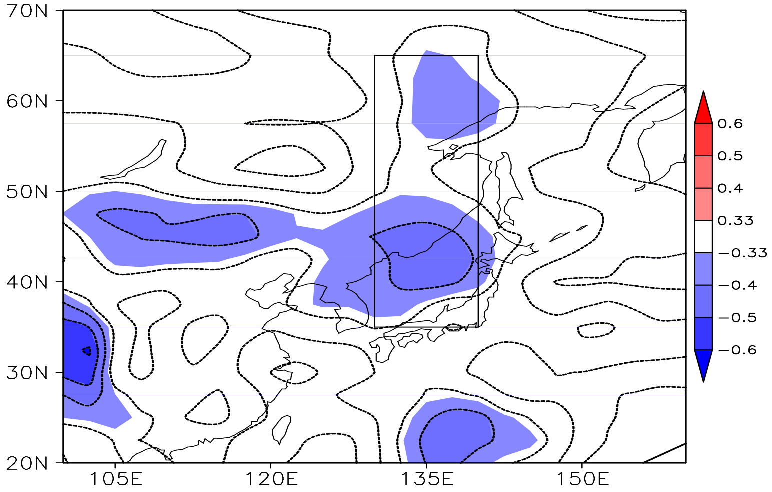

**Figure 2. The CC between WHD$_{NCP}$ DY and TS DY in autumn from 1980 to 2013. The shades indicate that the CC exceeded the 95% confidence level, and the rectangle represents the selected region (35–65°N，130–140°E) of predictor $x_1$.**

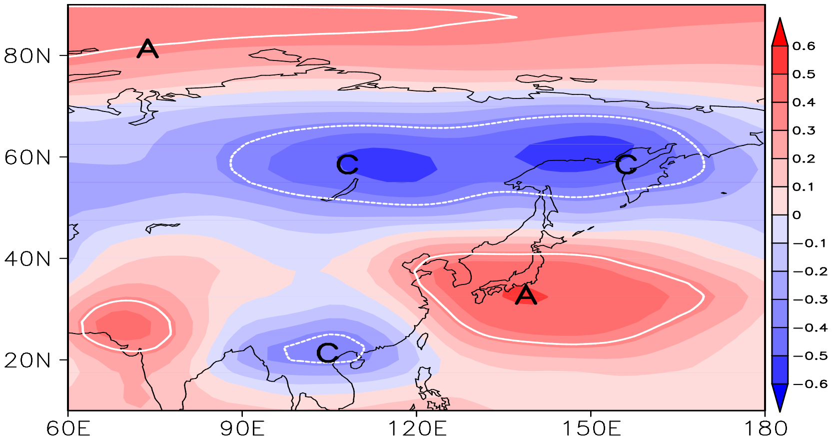

350 **Figure 3. The CC between predictor $x_1$ (×−1) and Z500 DY in winter from 1980 to 2013. The white curves indicate that the CC exceeded the 95% confidence level. A and C represent anti-cyclone and cyclone, respectively.**

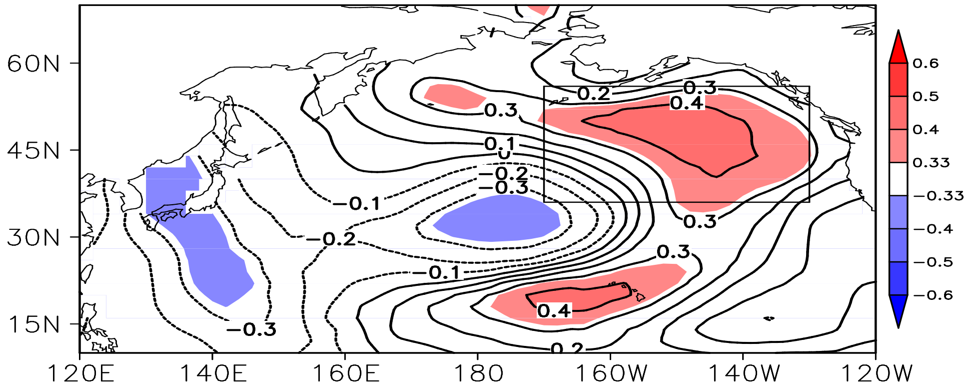

**Figure 4. The CC between WHD$_{NCP}$ DY and Pacific SST DY in autumn from 1980 to 2013. The shades indicate that the CC exceeded the 95% confidence level, and the rectangle represents the selected region (36–56°N, 130–170°W) of predictor $x_2$.** 355

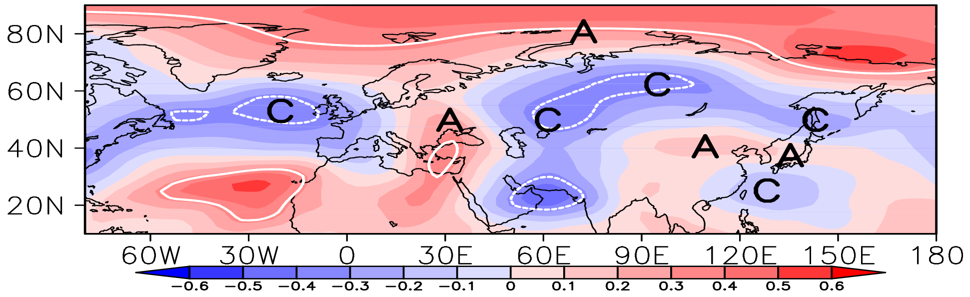

**Figure 5. The CC between predictor $x_2$ and Z500 DY in winter from 1980 to 2013. The white curves indicate that the CC exceeded the 95% confidence level. A and C represent anti-cyclone and cyclone, respectively.**

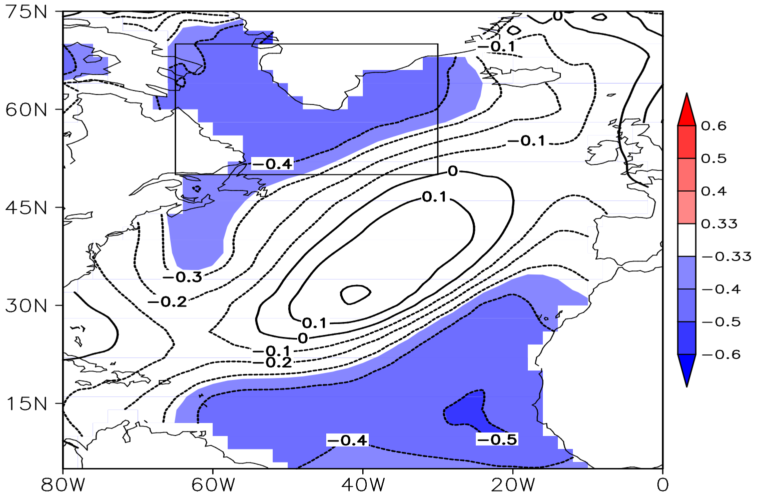

360 **Figure 6. The CC between WHD$_{NCP}$ DY and Atlantic SST DY in autumn from 1980 to 2013. The shades indicate that the CC exceeded the 95% confidence level, and the rectangle represents the selected region (50–70°N，30–65°W) of predictor $x_3$.**

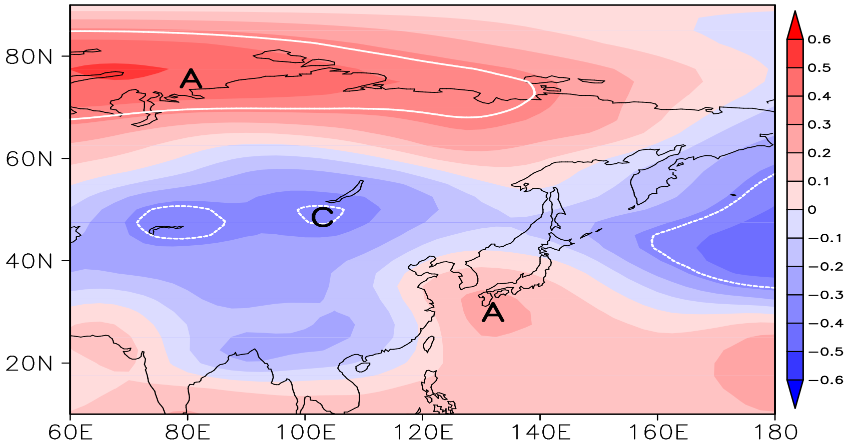

**Figure 7. The CC between predictor $x_3$ (×−1) and Z500 DY in winter from 1980 to 2013. The white curves indicate that the CC**
365 **exceeded the 95% confidence level. A and C represent anti-cyclone and cyclone, respectively.**

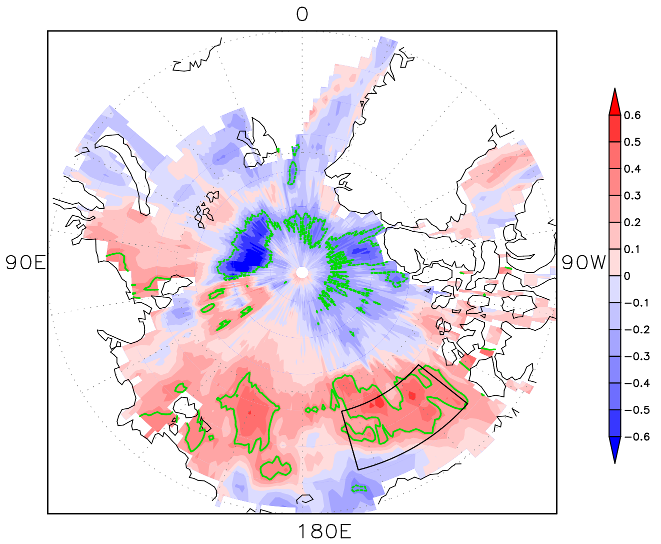

370 **Figure 8. The CC between WHD$_{NCP}$ DY and ASI DY in autumn from 1980 to 2013. The shades indicate that the CC exceeded the 95% confidence level, and the rectangle represents the selected region (73–78°N，130–165°W) of predictor $x_4$.**

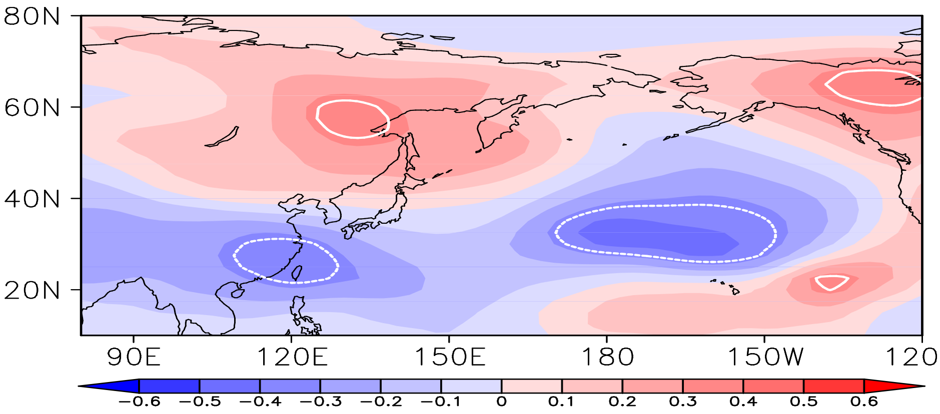

**Figure 9. The CC between predictor $x_4$ and Z500 DY in winter from 1980 to 2013. The white curves indicate that the CC exceeded the 95% confidence level.** 375

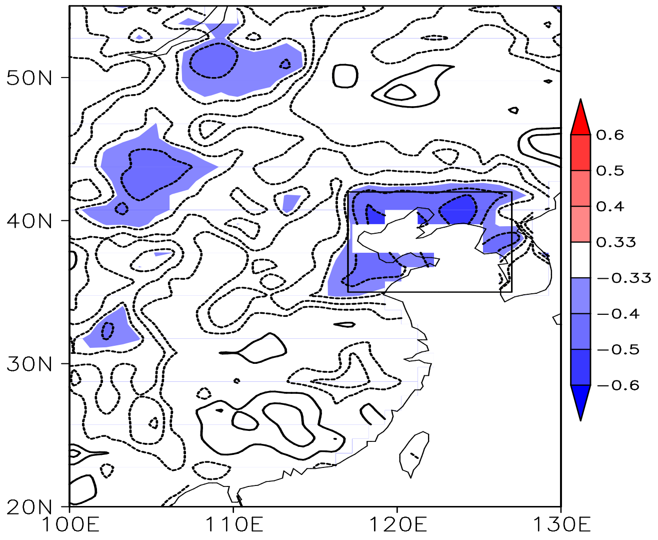

**Figure 10. The CC between WHD$_{NCP}$ DY and SoilM DY in autumn from 1980 to 2013. The shades indicate that the CC exceeded the 95% confidence level, and the rectangle represents the selected region (35–42°N，117–127°E) of predictor $x_5$.**

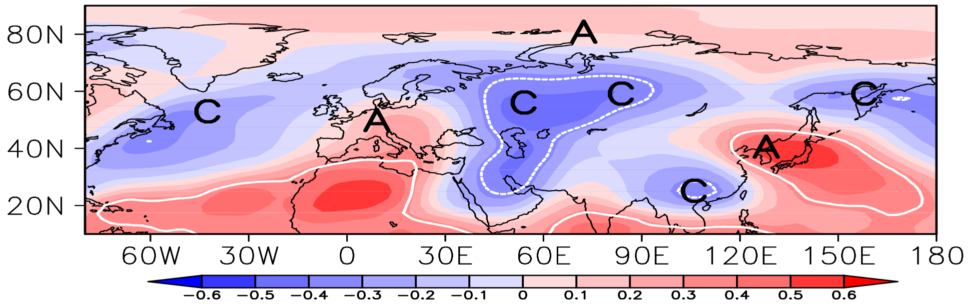

**Figure 11. The CC between predictor $x_5$ (×−1) and Z500 DY in winter from 1980 to 2013. The white curves indicate that the CC exceeded the 95% confidence level. A and C represent anti-cyclone and cyclone, respectively.**

Atmos. Chem. Phys. Discuss., doi:10.5194/acp-2016-691, 2016
Manuscript under review for journal Atmos. Chem. Phys.
Published: 16 August 2016

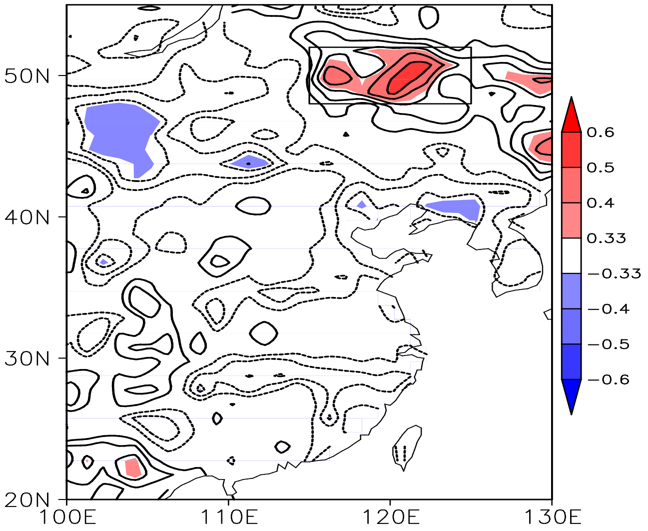

**Figure 12. The CC between WHD$_{NCP}$ DY and SoilM DY in summer from 1980 to 2013. The shades indicate that the CC exceeded the 95% confidence level, and the rectangle represents the selected region (48–52°N，115–125°E) of predictor $x_6$.**

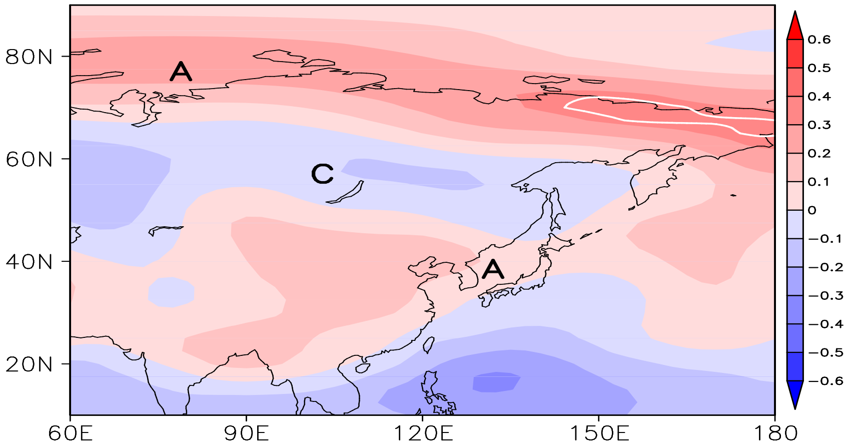

385

**Figure 13. The CC between predictor $x_6$ and Z500 DY in winter from 1980 to 2013. The white curves indicate that the CC exceeded the 95% confidence level. A and C represent anti-cyclone and cyclone, respectively.**

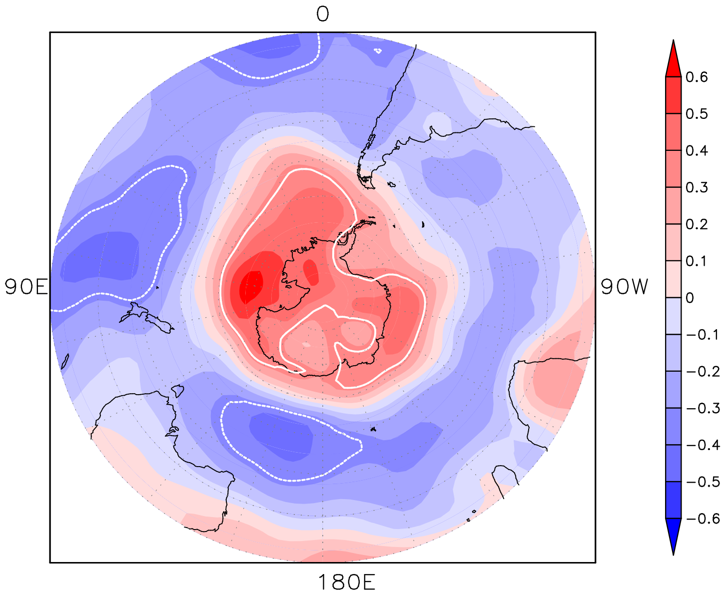

**Figure 14. The CC between WHD$_{NCP}$ DY and Sep–Oct Z850 DY from 1980 to 2013. The white curves indicate that the CC**

390 **exceeded the 95% confidence level.**

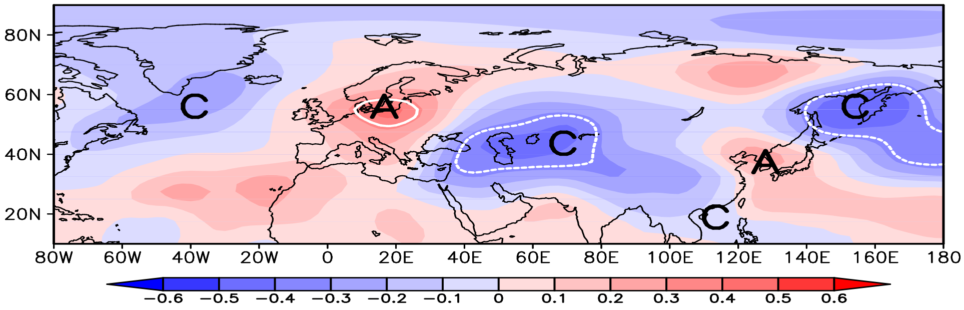

**Figure 15. The CC between predictor $x_7$ (×−1) and Z500 DY in winter from 1980 to 2013. The white curves indicate that the CC exceeded the 95% confidence level.**

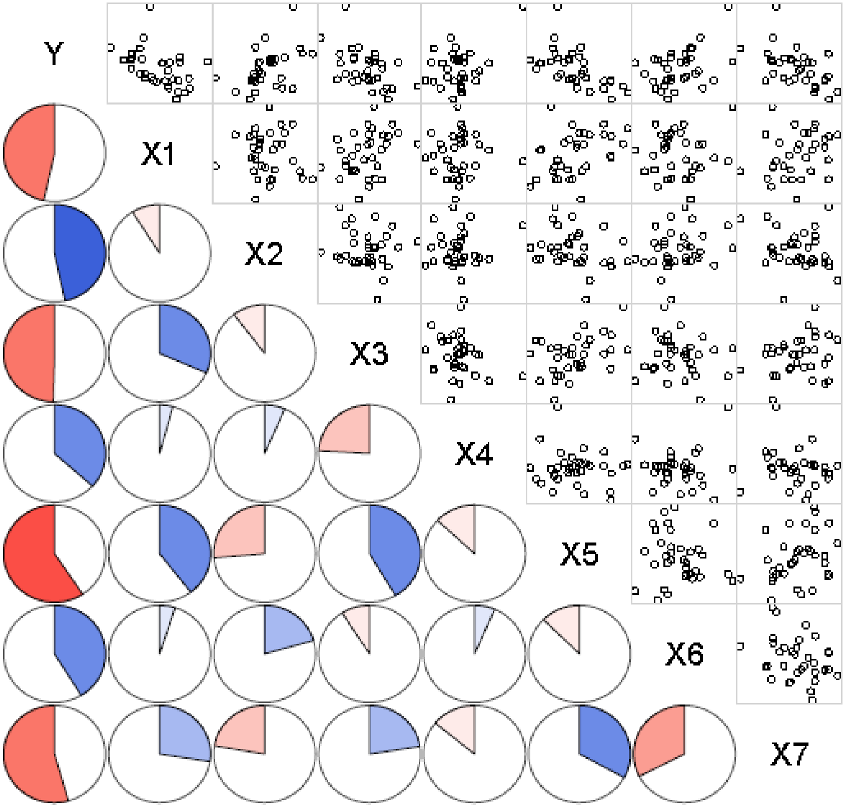

395 **Figure 16. Correlogram of the dependent (Y) and independent ($x_1, x_2 \ldots, and\ x_7$) variables, whose names were written on the diagonal. The lower panel shows the pie charts of correlation coefficients, representing the values by area and saturation, and showing positive/negative sign by blue/red, respectively. The upper panel shows the scatter plots.**

Atmos. Chem. Phys. Discuss., doi:10.5194/acp-2016-691, 2016
Manuscript under review for journal Atmos. Chem. Phys.
Published: 16 August 2016

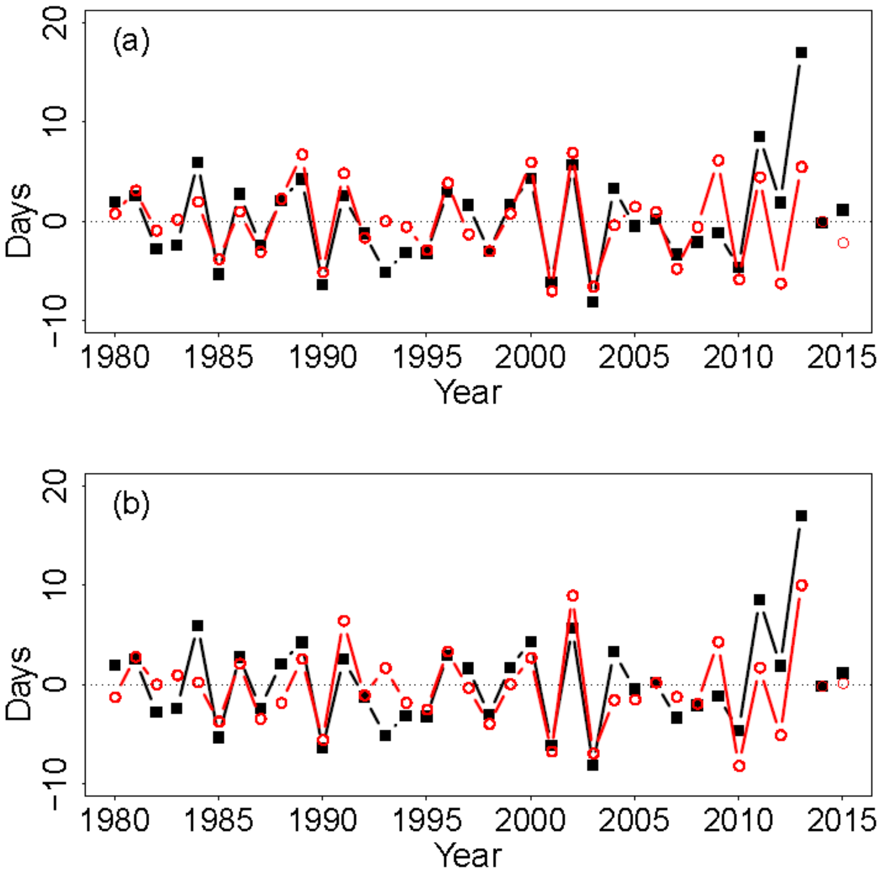

400 **Figure 17. The temporal variation of measured (black) WHD$_{NCP}$ DY, MLR (red, a) and GAM (red, b) cross-validation fitted WHD$_{NCP}$ DY from 1980 to 2013. The results for 2014 and 2015 represent the measured (black square) and predicted (red hollow circle) WHD$_{NCP}$ DY.**

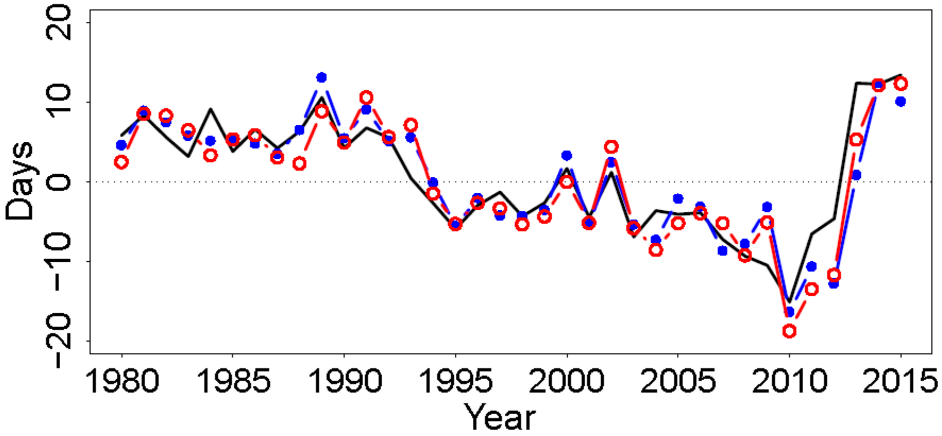

405 **Figure 18. The temporal variation of measured (black) $WHD_{NCP}$ anomaly from 1980 to 2015, MLR (blue) and GAM (red) simulative $WHD_{NCP}$ anomaly, which was composed of cross fitted series from 1980 to 2013 and predicted values in 2014 and 2015.**